ACS OMEGA

http://pubs.acs.org/journal/acsodf

Article

Influence of Ag on the Structural, Electrochemical, Antibacterial, and Photocatalytic Performance of the (CuO−Cu_2O)Cu Nanocomposite

B. Uma, Kurupalya Shivram Anantharaju,* B. S. Surendra,* K. Gurushantha, Sunil S. More, S. Meena, B. Hemavathi, and H. C. Ananda Murthy*

Cite This: *ACS Omega* 2023, 8, 9947−9961

Read Online

ACCESS | Metrics & More | Article Recommendations

ABSTRACT: The cost-effective novel Ag-doped (1−7%) (CuO−Cu_2O) Cu (C3) heterostructured nanocomposites are successfully synthesized by the facile solution combustion process using the *Leucas aspera* extract as a green fuel. The structural properties of fabricated nanocomposites were well-characterized by specific spectral techniques for enhanced electrochemical sensor detection, antibacterial activities, and sunlight-driven photocatalytic dye decoloration studies. The existence of Ag^+ ions has been confirmed by the appearance of two peaks of Ag $3d_{5/2}$ (367.9 eV) and Ag $3d_{3/2}$ (373.9 eV), with the chemical binding nature and exchange of the Ag^+ state in the nanocomposite lattice as revealed by X-ray photoelectron spectroscopy analysis. The energy band gap value of the doped nanocomposite decreases from 2.2 to 1.8 eV, as measured by the UV−visible absorption spectral technique, hindering the recombination of electron−holes pairs by trapping e^- and h^+. This result supports that the C3Ag5 nanocomposite has a great potential as a sunlight photocatalyst toward the Alizarin Red (AR) dye, for which an excellent degradation activity of 98% at 180 min was achieved compared to that of the host nanocomposite (78% at 180 min). The variation of redox peak potentials of the prepared graphite nanocomposite working electrode is an effective tool for paracetamol sensing activity in 0.1 M KCl using electrochemical spectral studies. In addition, the antibacterial activities of the C3Ag5 nanocomposite against *Escherichia coli* and *Staphylococcus aureus* were successfully studied. The C3Ag5 nanocomposite exhibited a better performance than C3. The increase in activity is attributed to the presence of Ag as a dopant.

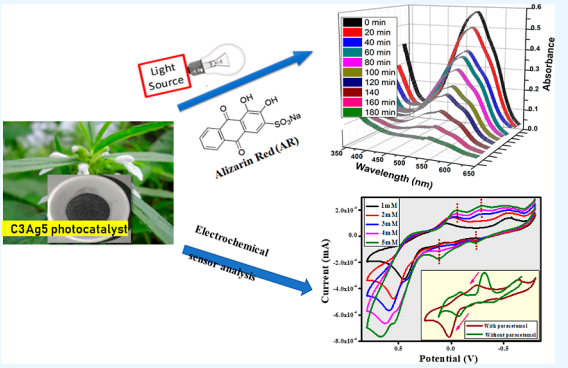

1. INTRODUCTION

Water is essential to all living things on the planet. Its demand is growing every day as a result of population increase, and it is becoming a serious difficulty that must be addressed in order to ensure a sustainable civilization. Rapid industrial development and excessive population growth have altered the natural composition of water by introducing various pollutants.[1] The development of effective technology to remove home and industrial pollutants before they enter the environment has been the subject of intense research and management. Filtration, adsorption, evaporation, and chlorination are all time-consuming and risky to the health and require expensive water treatment procedures that can sometimes result in secondary pollution.[2] As a result, new technologies for the removal of hazardous substances from water supplies have been created. The advanced oxidation method was originally created for the treatment of drinking water, and it is adapted for the treatment of wastewater from many sources due to its efficiency and effectiveness. Electrochemical oxidation, supercritical water oxidation, the Fenton reaction, ozone oxidation, heterogeneous photocatalysis using hydrogen peroxide, and wet air oxidation are examples of advanced oxidation methods.[3]

Heterogeneous photocatalysis is a strong choice among these modern oxidation techniques because of its low cost, chemical and biological inertness, and remarkable capacity to remove organic pollutants, colors, and allergens from wastewater. The mechanism of heterogeneous photocatalysis is primarily defined by the semiconductor's ability to create charge carriers in the presence of sunlight, followed by the formation of free radicals such as OH, which leads to subsequent reactions, eventually creating CO_2 and H_2O.[4] For

Received: November 4, 2022
Accepted: March 1, 2023
Published: March 10, 2023

https://doi.org/10.1021/acsomega.2c07124
ACS Omega 2023, 8, 9947−9961

efficient photocatalytic degradation of organic molecules, a variety of materials/agents such as simple metal oxides, complex oxides, transition metal oxides, and nitrides are available. Among these, CuO is a very good choice as a semiconductor photocatalyst because of its easy and cheap synthesis and non-toxicity.[5] It also possesses high excitation binding energy, high conductivity, good thermal stability, and excellent optical and electrical properties.[6] It is a p-type semiconductor with a small band gap of 1.2 eV. It is used in electrical cathode materials, glucose sensors, gas sensors, supercapacitors, solar cells, field emitters, and catalysts, among other applications.[7] It has strong antimicrobial characteristics and can also be used as a photocatalyst in wastewater treatment. It is also a popular heterogeneous catalyst for turning hydrocarbons into carbon dioxide and water.

Previous research has demonstrated that doping CuO with transition metals such as Ni, Cr, Cu, Mo, Fe, and Au improves photocatalytic activity by preventing photo-induced electron−hole recombination.[8] Silver doping of semiconductor nanoparticles is said to improve their photocatalytic performance.[9] Nanomaterials containing silver have long been known to have antibacterial properties. In a bacterial, fungal, and viral investigation, the silver ion has the highest biocidal efficiency.[10] Metallic silver nanoparticles have attracted a lot of attention in recent years due to their exceptional antibacterial properties. The photocatalytic efficiency of CuO is further enhanced if it is in the form of a heterostructure like $CuO/Cu_2O/Cu$ compared to that of a single phase compound.[11] The advantages of green syntheses over chemical and physical approaches include the following: environmental friendliness, affordability, and ease of scaling up for large-scale nanoparticle synthesis.[12] In addition, there is no need to utilize harmful chemicals and high temperatures, pressures, or energies. There are numerous methods that can be used to synthesize nanostructured materials with controlled shape, size, and structural characteristics.[13] A large number of the reactants, starting materials, stabilizers, and solvents utilized in the majority of wet chemical pathways are toxic and possibly dangerous.[14] Thus, plant-based bio-mediated synthesis methods are nearly risk-free while also being commercially and environmentally beneficial.

Leucas aspera is selected in the present investigation as it is widely distributed in India and has antipyretic, anti-venom, antibacterial, and pesticide capabilities.[15] The antibacterial effects of *L. aspera* extracts against *Vibrio cholerae*, *Escherichia coli*, *Salmonella typhi*, Klebsiella aerogenes, *Staphylococcus aureus*, *Proteus vulgaris*, and *Pseudomonas pyocyanea* have been shown in previous investigations using an aqueous leaf extract.[16] It is scarce to find research articles on doped copper-based nanocomposites in the literature. In this study, we synthesized the C3Ag5 nanocomposite using the *L. aspera* leaf extract as a reducing and stabilizing agent and assessed its antibacterial efficacy, photocatalytic activity, and supercapacitance behavior.

In the current study, we synthesized the C3Ag5 nanocomposite using the *L. aspera* extract as a fuel by the solution combustion method. Further, it was characterized to establish their nanoscale level composition. It was discovered that Ag has altered the crystallinity, band gap, crystallite size, charge carrier dynamics, and surface morphology of the C3 nanocomposite. To investigate the role of the structural, electronic, and surface properties of the doped compound, we conducted photocatalytic decolorization of the Alizarin Red (AR) dye and assessed the super-capacitance behavior and antibacterial activity against Gram-positive *S. aureus* and Gram-negative *E. coli* bacteria.

2. EXPERIMENTAL SECTION

2.1. Preparation of (CuO/Cu_2O) Cu and Ag-Doped (CuO/Cu_2O) Cu by the Solution Combustion Method. $Cu(NO_3)_2{\cdot}3H_2O$ and *L. aspera* extract as a fuel were considered in stoichiometric ratios and were placed in a crucible to synthesize $(CuO-Cu_2O)Cu$ by a low-temperature solution combustion route. All the chemicals were acquired from Merck, were of analytic grade, and were utilized without further purification. $Cu(NO_3)_2$ was used as an oxidizer, and an optimized quantity of *L. aspera* extract was used as fuel. A solution of selected materials and a minimal amount of water was then placed inside a preheated muffle furnace at 450 °C. The combustion process was initiated with an evaporation of the water content, and the liberation of a greater volume of CO_2 and N_2 gases was observed. The formed $(CuO-Cu_2O)$ Cu nanomaterial was foam in nature, brought down to room temperature, and dried. The resulted product is named as C3.

The solution combustion method was applied thereafter following the aforementioned procedure to synthesize 1, 3, 5, and 7 mol % Ag-doped $(CuO/Cu_2O)Cu$ (C3Ag) heterostructure nanocomposites by using $AgNO_3$ as a precursor from Sigma Aldrich, and they were labeled as C3Ag1, C3Ag3, C3Ag5, and C3Ag7 nanocomposites, respectively. The schematic experimental representation of synthesized C3Ag nanocomposites is shown in Figure 1.

2.3. Photocatalytic Measurement. The specific amount of synthesized nanomaterial (20 mg) was placed in a larger glass beaker containing 40 ppm AR dye solution. The photocatalytic test was carried out individually for both host C3 and Ag-doped C3 photocatalysts for around 180 min under

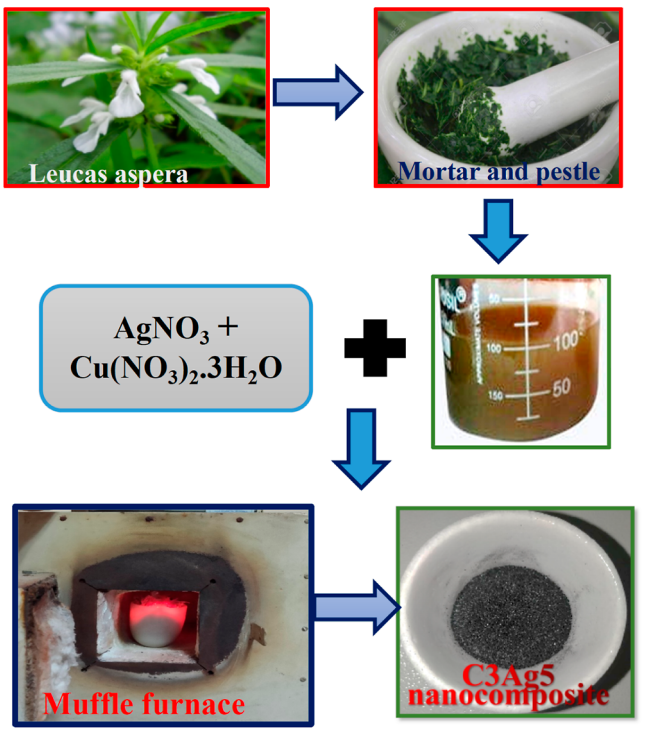

Figure 1. Schematic experimental representation of synthesis of the C3Ag5 nanocomposite by a facile combustion route.

https://doi.org/10.1021/acsomega.2c07124
ACS Omega 2023, 8, 9947−9961

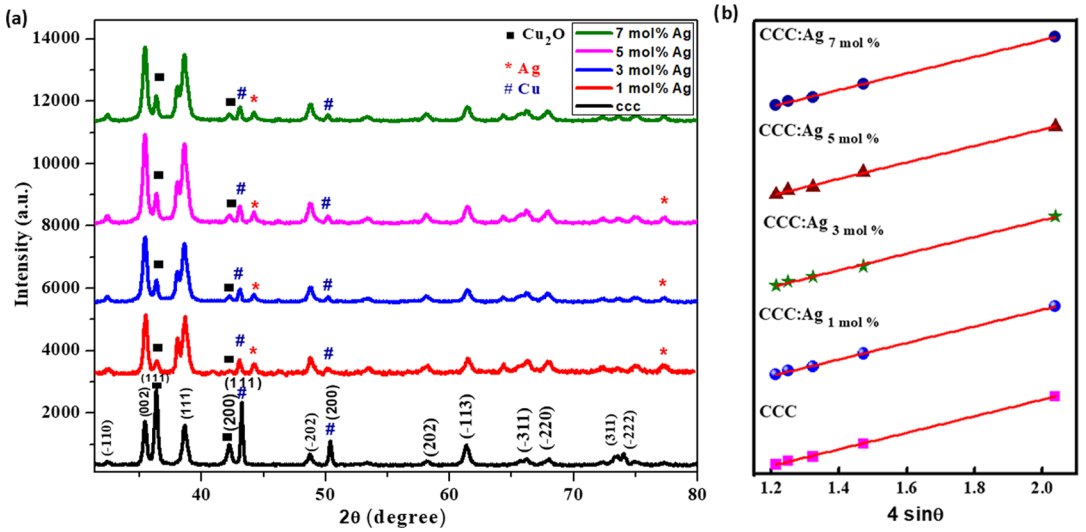

Figure 2. (a)PXRD pattern and (b) enlarged portion of (002), (111), and (111) peaks of C3 and the C3-Ag5 nanocomposite.

Table 1. Crystallite Size (Debye Scherrer's and W−h Plot Method) and Other Structural Parameters of C3Ag (0−7 mol %) Nanoparticles

	crystallite size (nm)				
CCC: Ag NPs (mol %)	Scherrer's Method	W−h plot method	stress × 10^{-3}	dislocation density × 10^{17} linm^2	structural factor × 10^{-3}
0	55	57	1.493	0.3305	4.487
1	19	20	1.563	2.77	4.477
3	20	21	1.662	2.5	4.484
5	16	18	1.752	3.906	4.467
7	21	22	1.685	2.5	4.483

natural sunlight irradiation. This photocatalytic reaction was carried out between 11 am and 2 pm to prevent the fluctuations in the intensity of sun rays. 5 mL of dye solution was removed at regular intervals to track the change in absorption intensity. Our prior work[17] thoroughly revealed the procedure to conduct the photocatalytic experiment under sunshine. All the experiments were done in triplicate with errors of less than 3%, and the average value was reported.

2.4. Electrochemical Measurement. The mixtures of the synthesized nanoparticle, graphite, and as a binder silicon oil were taken in a mortar of ratio 1:3:1 and ground (∼30 min) to get a paste. Then, in a Teflon tube, the paste was filled without any air gap. Lastly, to avoid the production of uneven surfaces/gaps/holes, the filled Teflon tube was smoothened over wax paper. For the electrical contact, a copper wire was cautiously inserted on one side of the tube and made as one among the three-electrode system for the electrochemical measurements.

2.5. Antibacterial Performance. Petri plates containing 20 mL of Muller−Hinton agar were seeded using a cotton swab with 24 h (old) culture of the *E. coli* and *S. aureus* strains. Sterile discs (5 mm diameter) are plated on the plate with 3.0 mg/mL concentrations of the test sample and standard. The plates were then incubated at 37 °C for 24 h. The antimicrobial activity was assayed by measuring the diameter of the inhibition zone formed around the well using Ciprofloxacin as a positive control.

3. RESULTS AND DISCUSSION

3.1. Powder X-ray Diffraction Analysis. The synthesized C3 and Ag-doped C3 (1−7 mol %) were analyzed by X-ray diffraction (XRD) to confirm the structural properties of the samples. Figure 2a shows the diffraction peaks of C3 at 2θ = 32.5, 35.4, 38.6, 48.7, 53.2, 58.0, 61.3, 66.2, 68.0, 73.4, and 74.2 that correspond to (−110), (002), (111), (−202), (202), (−113), (−311), (−220), (311), and (−222) planes of monoclinic CuO diffraction planes, which well matches to the JCPDS card (no.: 45−0937). The reflections present at angles 36.4 and 42.1 were due to the (111) and (200) planes, respectively, of the Cu_2O phase (JCPDS File no. 5-661 and 5-667). Minute additional peaks were noted for the (1−7) mol % of Ag at 44.5 and 77.2 2θ diffraction angles pointing toward the (220) and (311) planes of metallic silver (Figure 2a).[18] Powder XRD (PXRD) results verified that favored products are formed such as CuO, Cu_2O, metallic copper, and metallic silver.

Notably, the diffraction planes have variation in peak intensities for the different contents of Ag in C3 (Figure 2a). This is probably due to the change in the crystalline orientation in terms of microstructures or lattice disorder in the CuO/Cu_2O lattices.[19,20] The PXRD studies show that the transformation phase of Cu_2O to CuO in (CuO−Cu_2O)Cu along the planes (002) and (111) was promoted with the increase of Ag concentration. This change in intensity and phase transformation is due to the impact of the lower ionic radii of Cu^{2+} (0.072 nm) and Cu^{+} (0.077 nm) ions than the ionic radii of metallic of Ag (0.144 nm).[21] The different concentration of Ag dopants improves the crystal quality of CuO along the planes (002) and (111) but affects the crystal quality of the planes Cu_2O(111), metallic Cu(111) in terms of microstrain and stress (Figure 2b). The microstrain and stress was determined in order to confirm the change in the peak intensity of C3Ag5.[22,23]

https://doi.org/10.1021/acsomega.2c07124
ACS Omega 2023, 8, 9947−9961

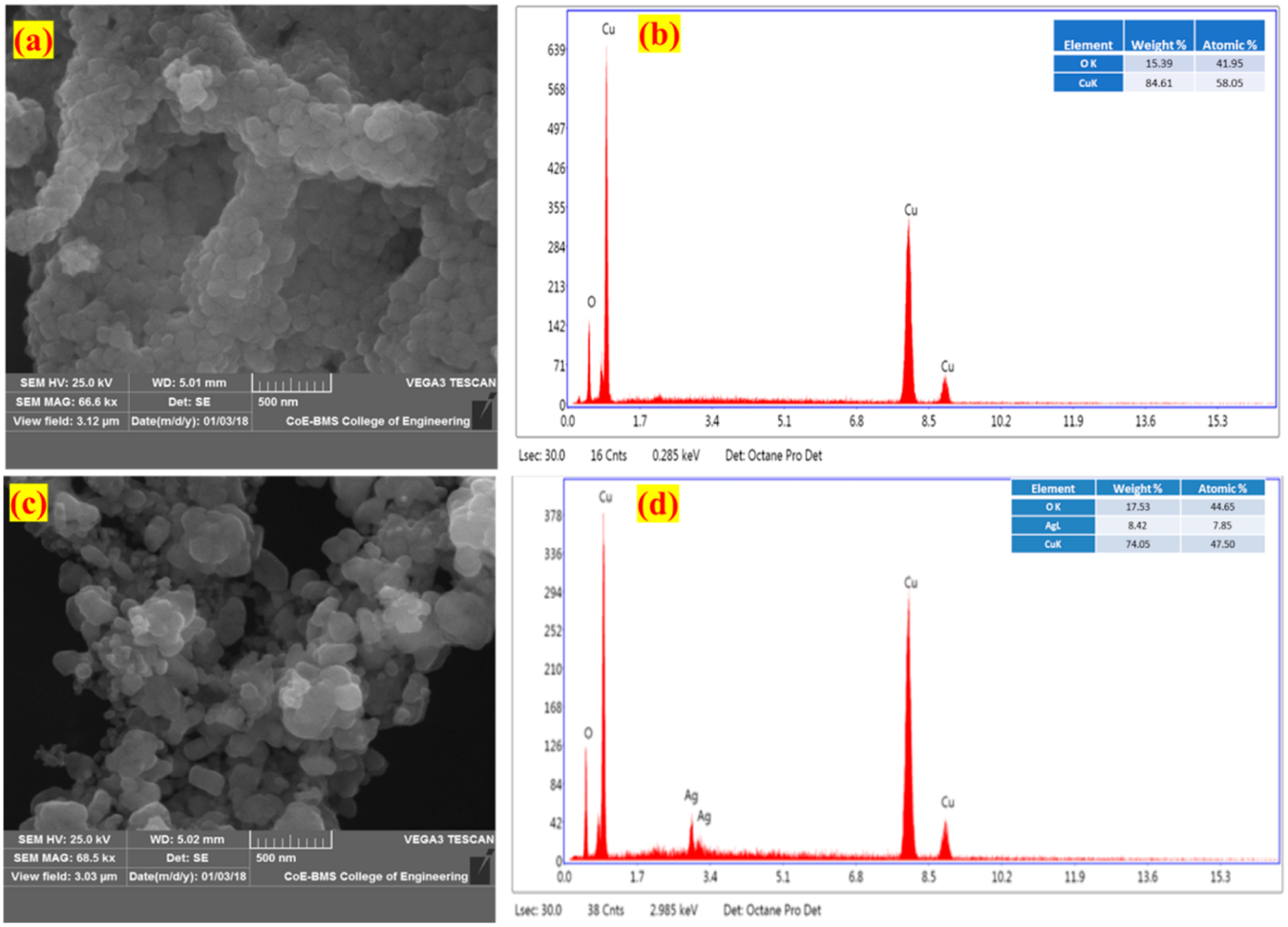

Figure 3. SEM-EDAX images of (a,b) C3 and (c,d) C3Ag5 nanocomposite.

The average crystal sizes of as-formed C3, C3Ag1, C3Ag3, C3Ag5, and C3Ag7 were in the range 16−55 nm, as achieved by using Scherrer's formula and presented in Table 1. It can also be seen that the 2θ peak positions of the major diffraction pattern after Ag doping of (CuO−Cu_2O)Cu had similar values to that of pristine (CuO−Cu_2O)Cu, except for the changes in the intensities of the peaks. As the Ag contents increase from 0 to 7 mol %, the broadening of the peaks corresponding to (002) and (111) planes of CuO gradually increases which indicates the smaller crystallite size of the material. It is observed that pristine C3 has an average size of 55 nm and it decreases up to 16 nm for 5 mol % Ag. Many researchers have synthesized Ag-doped CuO-based materials using various routes and optimized the particle size under different conditions. Figure 2b shows the William Hall plot of prepared nanocomposites obtained by plotting the $\beta \cos \theta$ values as a function of 4 sin θ. The crystallite size and lattice strain for both C3 and Ag-doped CCC were determined by W·H calculation (eq 1) and are listed in Table 1.[24] Here, β is the full width at half maximum (FWHM), D is the crystallite size, and ε is the strain.

$$\beta \cos \theta = k\lambda/D + 4\varepsilon \sin \theta \quad (1)$$

3.2. Scanning Electron Microscopy and Energy-Dispersive X-ray Spectroscopy Analysis. The scanning electron microscopy (SEM) examinations were performed to confirm the nature and surface morphology of the nanoparticles, as depicted in Figure 3a,c. The synthesized C3 nanoparticles had sizes that are in the nanometer range, and their structures were homogeneous and spherical that were agglomerated in nature. The agglomerated particle structure is due to densification caused by the narrow space between the particles (Figure 3a). Figure 3c shows the micrograph of C3Ag5 with 500 nm scale magnification. The image indicates that only few nanoparticles have a spherical shape, few have a flower-like morphology, and some nanoparticles are well separated from each other, while most are present in the agglomerated form and not shaped homogeneously. The allotment of the Ag dopant decreases in crystallite size due to separation and the change of the particle structure. Fairly different from that of the host C3, Ag-doped C3 samples exhibit a distinguishable morphology. Thus, the significant influence in the growth pattern is evidenced upon Ag doping, as also supported by the average crystallite size value calculated from PXRD.

Figure 3b,d shows the chemical constituents present in prepared host and Ag-doped CuO samples, which were examined by energy-dispersive X-ray spectroscopy (EDAX). The EDAX spectral analysis validates the purity of C3 and C3Ag5-doped samples. The pattern (Figure 3b) clearly indicates the presence of Cu and O in the spectrum and the elements like Cu, O, and Ag are detected from the observed spectrum in Figure 3d, which indicates the specific doping with the absence of other impurities in Ag-doped CuO samples.

https://doi.org/10.1021/acsomega.2c07124
ACS Omega 2023, 8, 9947−9961

3.3. Transmission Electron Microscopy Analysis.

Figure 4a,b depicts the transmission electron microscopy (TEM) images of C3-Ag5 nanoparticles at different magnifications. The reported micrographs clearly express the formation of agglomerated irregular shaped nanoparticles. Figure 4c shows the high-resolution TEM (HRTEM) image of prepared C3Ag5, and Figure 4d clearly indicates the lattice planes with d-spacings of 0.2449, 0.2501, 0.2071, and 0.144 nm corresponding to (111), (002), (111), and (220) planes of Cu_2O, CuO, metallic copper, and metallic silver, respectively. The crystallite size calculated from the TEM analysis matches well with the crystallite size estimated from Scherrer's method. The appearance of the ring pattern in the selected area electron diffraction (SAED) results shows the high crystallinity of the sample (Figure 4e). These rings match well with the (−113), (111), and (002) planes of CuO, the (111) plane of Cu_2O, and the (111) plane of metallic copper. TEM analysis further confirms the formation of C3Ag nanoparticles and the absence of other impurities.

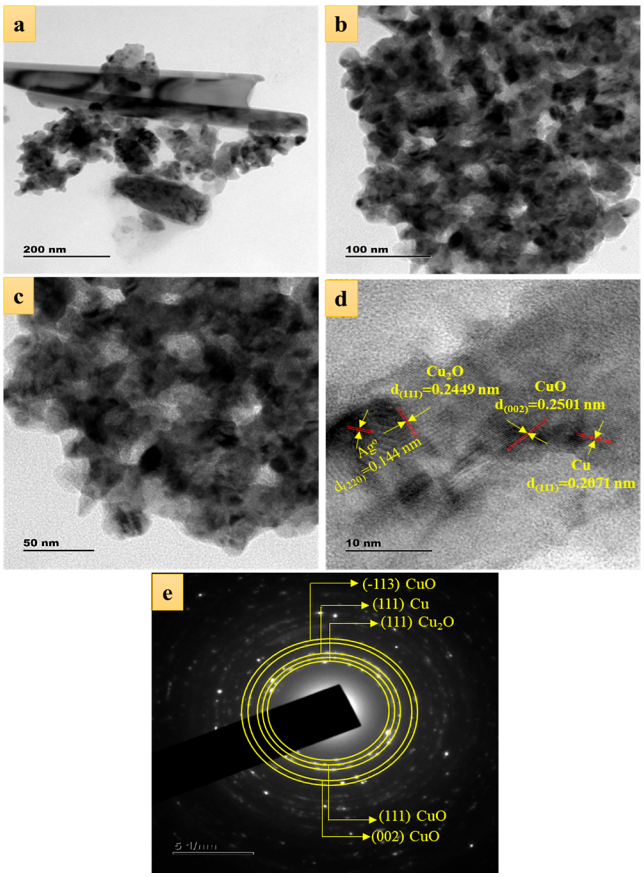

Figure 4. (a,b) TEM images at different magnifications, (c,d) HRTEM image, and (e) SAED pattern of the C3Ag5 nanoparticle.

3.4. X-ray Photoelectron Spectroscopy Investigation.

An X-ray photoelectron spectroscopy (XPS) study was performed to regulate the presence of Ag at the (CuO−Cu_2O)Cu surface as well as to examine their oxidation states. Figure 5a shows the survey of the sample for Cu, Ag, O, and C elements. The peak at 284.8 eV corresponded to adventitious carbon (Figure 5b). As shown by the O 1s in Figure 5c, the predominant peak of O 1s (529.7 eV) was assigned to the lattice oxygen, along with which a satellite peak is observed at 531.2 eV. Examining the XPS spectrum of Ag 3d (Figure 5d), the two peaks of Ag $3d_{5/2}$ (367.9 eV) and Ag $3d_{3/2}$ (373.9 eV) observed were attributed to metallic silver (Ag^0), which agrees well with previous reports,[25] confirming the existence of Ag nanoparticles in (CuO−Cu_2O) Cu. Further, it was slightly lower than the standard binding energy values ($3d_{5/2}$, 367.9 eV and $3d_{3/2}$, 373.9 eV), indicating that there was an interface interaction between CuO and Ag nanoparticles. The XPS result of Cu 2P of the sample shows peaks at 933.4 and 943.7 eV (Cu $2p_{3/2}$) and 953.4 and 962.1 eV (Cu $2p_{1/2}$) with the differences of 20 and 18.4 eV, respectively, which proves the formation of copper (II) oxide (Figure 5e).[26] In a previous study, the energy separation of ≥19.8 eV was observed in CuO and that of ≤19.8 eV was observed in either pure metallic Cu or Cu_2O.[27] However, chemical state differentiation of Cu was difficult to be found with XPS since the Cu 2p binding energies of Cu^+ and Cu metal were almost the same.[28] The presence of two satellite peaks at higher binding energies of 943.7 and 962.1 eV is typical of materials having a d9 configuration in their ground state, which obliviously shows the presence of Cu^{2+}.[29]

3.5. Diffuse Reflectance Spectral Analysis.

The optical properties of the synthesized host C3 and C3Ag5 nanocomposites were examined using UV−visible spectrophotometric techniques and are shown in Figure 6a,b. An increased absorption of the C3Ag5 photocatalyst was observed after doping of Ag ions compared to that of the host C3 nanocomposite in the visible light range of 400−800 nm (Figure 6a). The maximum intense peak was found for the C3Ag5 nanocomposite due to surface plasmon resonance of Ag.[30] The broad absorption band of the prepared host and doped nanocomposites were recorded in the wavelength range of 200 to 325 nm, and no absorption peaks were observed in the higher wavelength of 325 to 800 nm. The reflectance spectral of C3 and C3Ag5 photocatalysts were recorded in the range between 200 and 800 nm as shown in Figure 6b. The energy band gap (E_g) of the prepared host and doped nanocomposites were calculated by plotting energy ($h\nu$) against $[F(R)h\nu]^2$ as elucidated from the Kubelka−Munk process (eq 2).[31]

$$F(R) = \frac{(1-R)^n}{2R} = \frac{K}{S} \tag{2}$$

The obtained energy band gap of the prepared host and doped nanocomposites were found to be 2.2 and 1.8 eV, respectively, as depicted in Figure 6c. Therefore, the prepared Ag-doped nanocomposites show a narrow energy band gap of 1.8 eV, representing the higher photoresponse in the visible light than that of the host C3 nanocomposite. The decrease in the energy band gap of prepared materials is commonly attributed to the d−d transitions of e^- and charge transfer transition across Ag ions, which provides sites to trap electrons and holes, which further inhibits the recombination of photon-generated carriers.[32,33] The band edge sites of C3 and C3Ag5 photocatalysts can be calculated by using eqs 3 and 4

$$E_{VB} = X - E_0 + 0.5E_g \tag{3}$$

$$E_{CB} = E_{VB} - E_g \tag{4}$$

Here, X is the electronegativity of the nanocomposite, E_g is the energy band gap, and E_0 is the energy of free electrons with respect to the standard hydrogen electrode for about 4.5 eV. The edge potentials E_{CB} and E_{VB} of C3 and C3Ag5

https://doi.org/10.1021/acsomega.2c07124
ACS Omega 2023, 8, 9947−9961

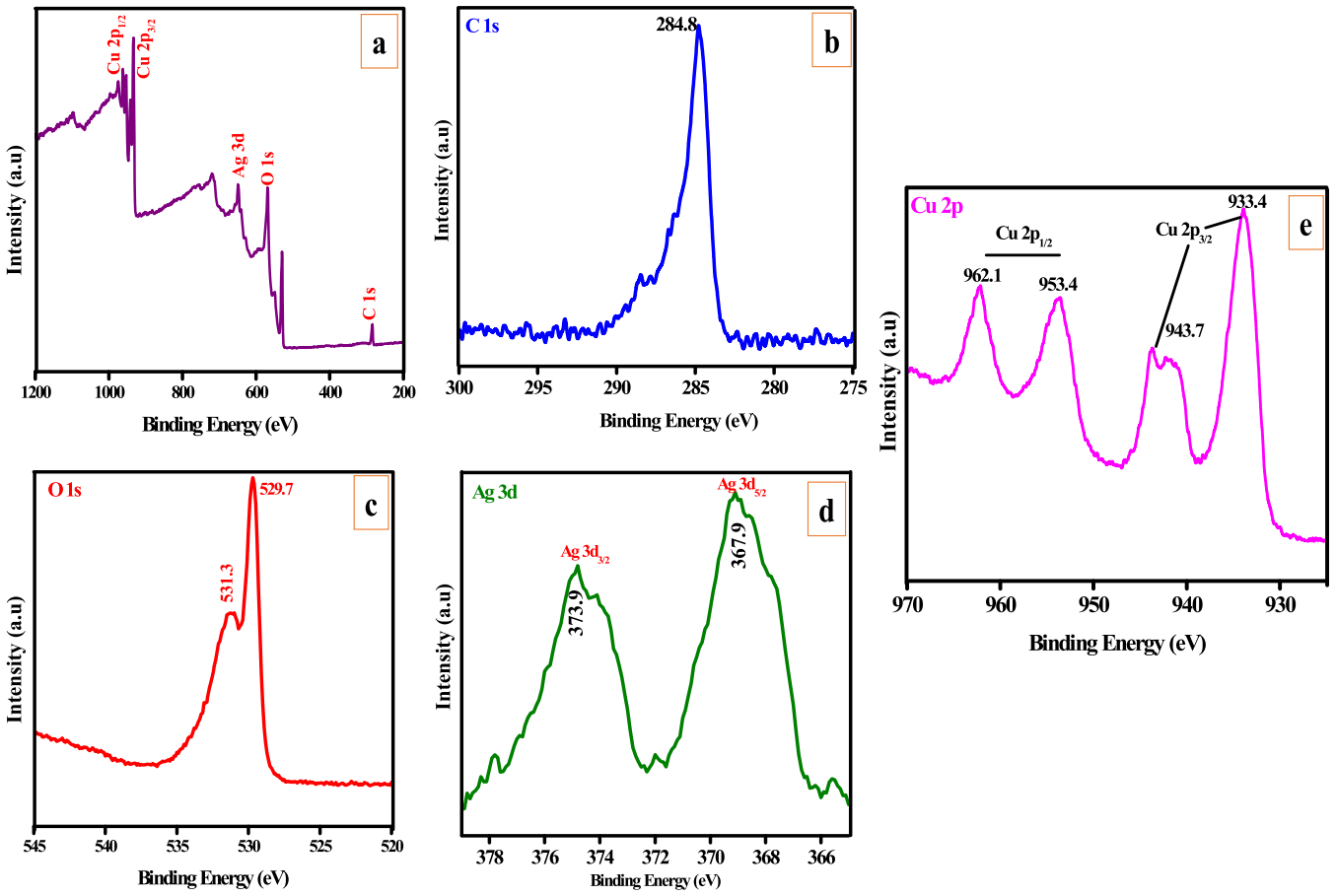

Figure 5. XPS spectra of the C3Ag5 sample and (a) wide spectral range, high-resolution XPS spectra of (b) C 1s, (c) O 1s, (d) Cu 2p, and (e) Ag 3d.

photocatalysts were calculated as −1.2 and 0.6 eV, respectively, with the help of the electronegativity (X) value of the prepared material found at 4.2 eV, and the edge potentials E_{CB} and E_{VB} of C3 photocatalysts were calculated as −1.9 and 0.3 eV, respectively. The obtained results showed the excellent photocatalytic application for the lower energy band gap of C3Ag5 photocatalysts compared to that of the C3 photocatalyst.

3.6. Fourier Transform Infrared Spectroscopy. The Fourier transform infrared (FTIR) spectrum of the C3Ag5 nanocomposite synthesized using the green mediated solution combustion method was recorded in the range 4000−400 cm^{-1} as shown in Figure 7. The presence of a strong peak at 3697 cm^{-1} attributed to hydroxyl (O−H) symmetric stretching vibration indicates the presence of a water molecule, and its asymmetric stretching vibrations was found at 2389 cm^{-1}.[34] The appearance of major peaks in the finger print region is associated to the metal−oxygen (M−O) vibration linkages. The bending vibrations of Cu−O, Ag−O, and Cu−O−Ag linkages were found to be 481, 562, and 659 cm^{-1}, respectively, as depicted in the inset of Figure 7.[35] The appearance of supplementary peaks at 1535 and 1652 cm^{-1} corresponds to stretching vibrations of Cu−O and Ag−O molecules, respectively.

3.7. Brunauer, Emmett, and Teller Analysis. The pore diameter and textural properties of the C3Ag5 nanocomposite prepared by the green mediated solution combustion method was examined by the Brunauer, Emmett, and Teller (BET) method. The solution combustion assisted nanocomposite normally shows a large surface area due to liberation of heat (exothermicity).[36] The BET surface area of the C3Ag5 nanocomposite was recorded to be 82 m^2/g, as depicted in Figure 8a. The larger surface area of the C3Ag5 nanocomposite is obtained by the impact of the uniform distribution of nanoparticles, as ascertained in SEM micrographs and Scherrer's method in XRD analysis. The mean pore diameter of this prepared sample was recorded to be 7.9140 nm, and the total pore volume is found to be 4.2108×10^{-3} cm^3 g^{-1}. The obtained results confirm that the C3Ag5 nanocomposite is mesoporous in nature. Figure 8b is the Barrett−Joyner−Halenda adsorption isotherm plot, which shows the pore diameter of the prepared C3Ag5 nanocomposite. This confirms that the prepared C3Ag5 nanocomposite has no pores in the macropore region (i.e., 500 Å), which means that pores are in the mesoporous region, and hence, the prepared material is mesoporous.[37,38]

4. PHOTOCATALYTIC STUDIES OF C3 AND C3AG5 NANOCOMPOSITES

Water is a fundamental component and essential to functioning for the known life on Earth. Currently, the toxicity of dye pollutants has been increasing by various divisions and creating major issues around the biosphere. These toxic effects from various dyes and their capacity to attack common water treatment actions have encouraged the scholars to implement an efficient and cost-effective environmentally friendly method

https://doi.org/10.1021/acsomega.2c07124
ACS Omega 2023, 8, 9947−9961

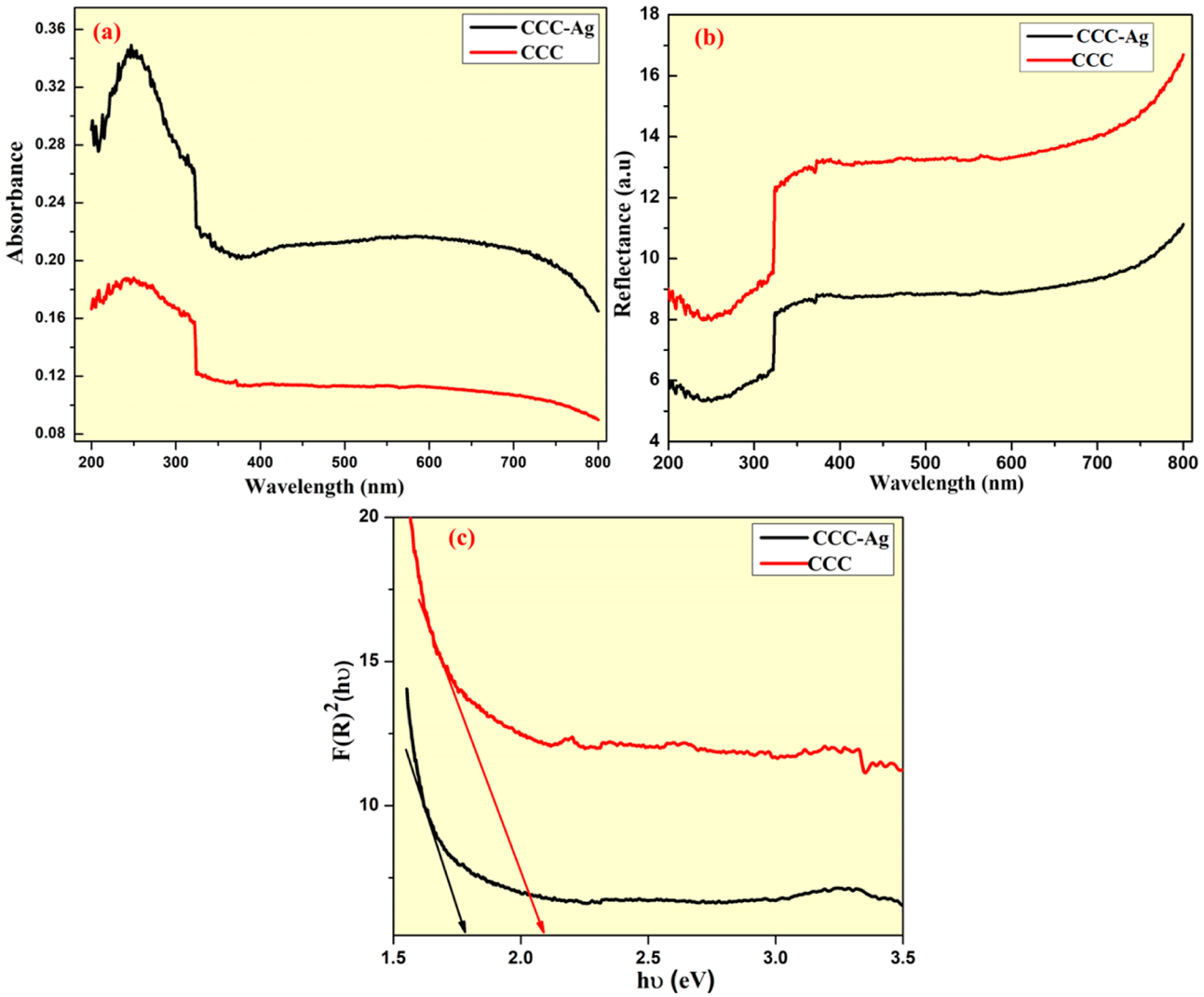

Figure 6. (a) Diffuse absorbance spectra of C3 and C3Ag5 nanocomposites; (b) reflectance spectral analysis; and (c) Kubelka–Munk plot transformed reflectance spectra for optical band gap calculations.

to reduce the toxic pollutant concentrations. Thus, the photocatalytic dye degradation studies are a potential technique for the treatment of several contaminated dye pollutants in water media.[39−41] In this research, we explored the photocatalytic dye degradation performance of prepared C3 and C3Ag5 nanocomposites on AR dye under the impact of visible light. The experimental photocatalytic dye decoloration activity was carried out for 40 ppm AR dye stock solution and 20 mg of prepared C3 and C3Ag5 nanocomposites under visible-light irradiation. The decoloration efficiency of the prepared C3 and C3-Ag nanocomposites on AR dye were analyzed by measuring the absorbance of collected dye solutions after every 15 min time intervals (Figure 9a,b). Thus, the photocatalytic dye degradation performance of AR dye has been increased due to the increase of light irradiation time in the presence of C3 and C3Ag5 nanocomposites. An excellent photocatalytic dye degradation activity was achieved, with a value of 98% at 90 min, for the C3Ag5 nanocomposite compared to that of the host C3 nanocomposite (78% at 90 min), as shown in Figure 9c. The standard error bar plot of AR dye degradation spectral studies is carried out under sunlight irradiation as given in Table 2. Also, the dye degradation performances on AR dye in the dark and under photolysis were recorded and found to be 9.8 and 13.2%, respectively (Figure 9c). The reusability and photostability of the prepared C3Ag5 nanocomposite on AR dye degradation was performed under similar conditions over five cycles (Figure 9d). After the first run, the used catalyst was recovered, washed using deionized water, heated to 40 °C for 20 min, and reused in subsequent degradation cycles. Further, the total organic carbon (TOC) analysis of the prepared C3Ag5 nanocomposite on AR dye was carried out as shown in Figure 9e. The results show that the percentage of TOC removal concentration decreased gradually with reaction time. The maximum TOC removal was 88% after 180 min of irradiation, which represents that most of the AR dye was mineralized during the photocatalytic process.

Further, the photocatalytic discoloration of AR dye studies was supported by scavenging assessments using different scavengers, and its absorption spectral analysis without and with scavengers was examined as shown in Figure 10. This examination was conducted to verify the photodiscoloration efficiency of AR dye using C3Ag5 nanocomposites. The experimental photocatalytic degradation analysis was carried out with acryl amide, ammonium oxalate, and isopropanol scavengers, yielding values of 89, 52, and 25%, respectively (Figure 10a−c). Also, the photocatalytic dye degradation was

https://doi.org/10.1021/acsomega.2c07124
ACS Omega 2023, 8, 9947−9961

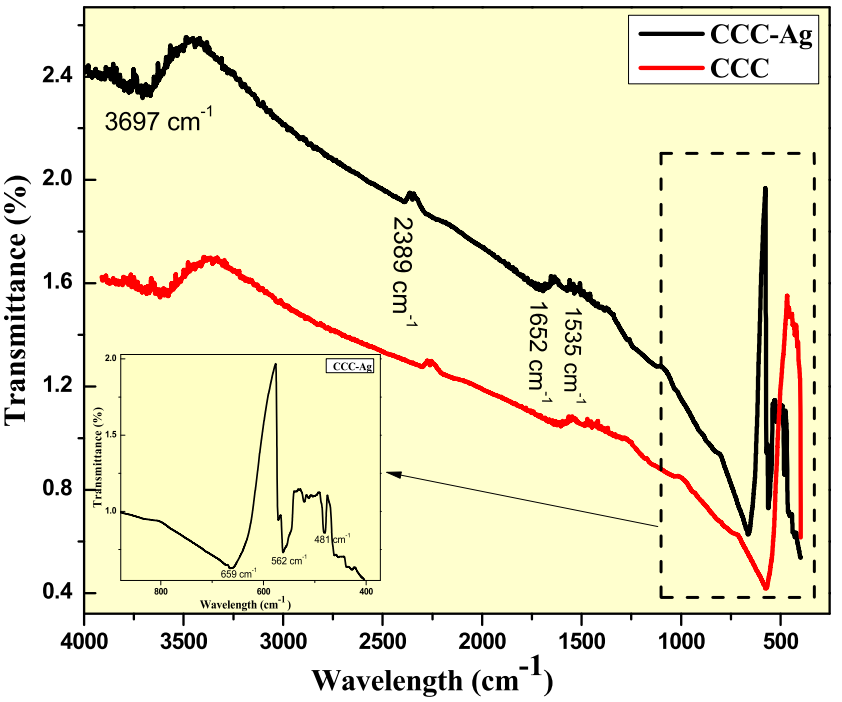

Figure 7. FTIR spectral analysis of (a) C3 and (b) C3Ag5 nanocomposites.

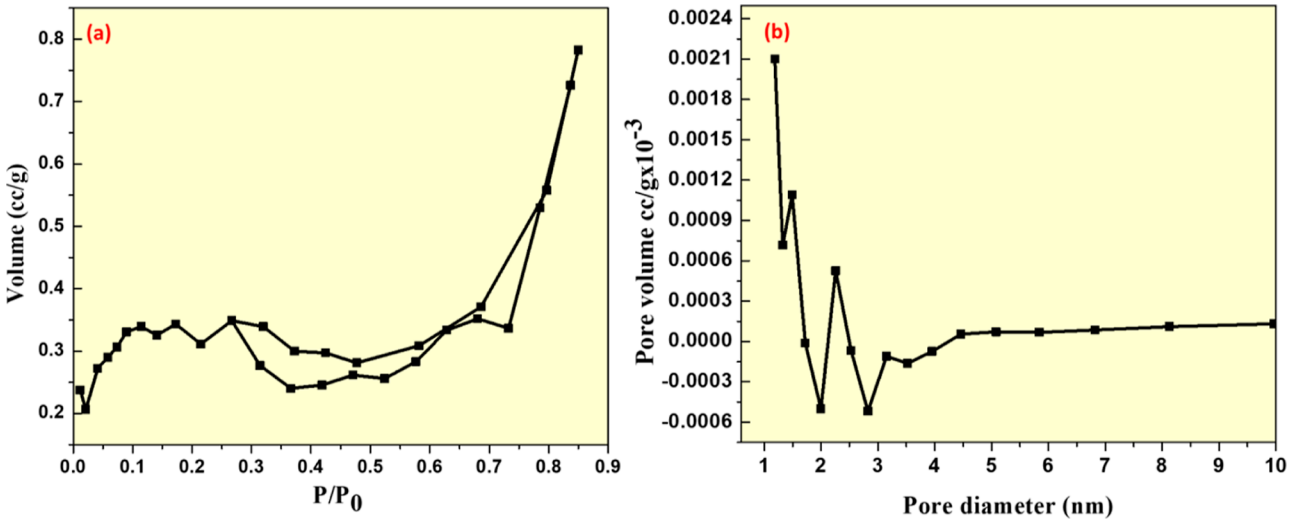

Figure 8. (a) N_2 adsorption and desorption isotherms and (b) pore volume distribution plot of the prepared C3Ag5 nanocomposite.

carried out in the absence of scavengers, which shows a value of 98% at 180 min (Figure 10d). In the scavenger experimental analysis, the isopropanol scavenger plays a dynamic role in photocatalytic degradation by blocking the holes, which confirms that holes (h^+) are mainly responsible for dye degradation. Therefore, photocatalytic degradation was successfully achieved by holes as an effective tool under sunlight irradiation.[42,43]

The possible mechanism of photocatalytic dye decoloration of C3Ag5 on AR dye under visible light irradiation is revealed in Figure 11. The impact of light energy on the prepared photocatalyst surface shows photosensitization of AR dye in irradiated visible light (eq 5). This process comprises equal numbers of electrons (e^-) and holes (h^+) moving from the valence band to the conduction band (eq 6). In the photocatalytic dye decoloration reaction, the water and oxygen molecules are directly influencing the formation of superoxide radicals ($O_2^{\bullet -}$) by the presence of e^- in the conduction band (eq 7) and hydroxyl radicals ($OH^{\bullet -}$) (eq 8) by the presence of holes in the valence band, respectively. The generated radicals play a vital role in the photocatalytic dye decoloration activities by braking of complex dye structures into eco-friendly byproducts.[44,45]

$$\mathrm{Ag(CuO - Cu_2O)Cu} + h\nu(\text{light energy}) \rightarrow \mathrm{Ag(CuOCu_2O)Cu^*}(\text{energy}) \quad (5)$$

$$\mathrm{Ag(CuO - Cu_2O)Cu^*}(\text{energy}) \rightarrow \mathrm{Ag(CuO - Cu_2O)Cu}(h^+ + e^-) \quad (6)$$

https://doi.org/10.1021/acsomega.2c07124
ACS Omega 2023, 8, 9947−9961

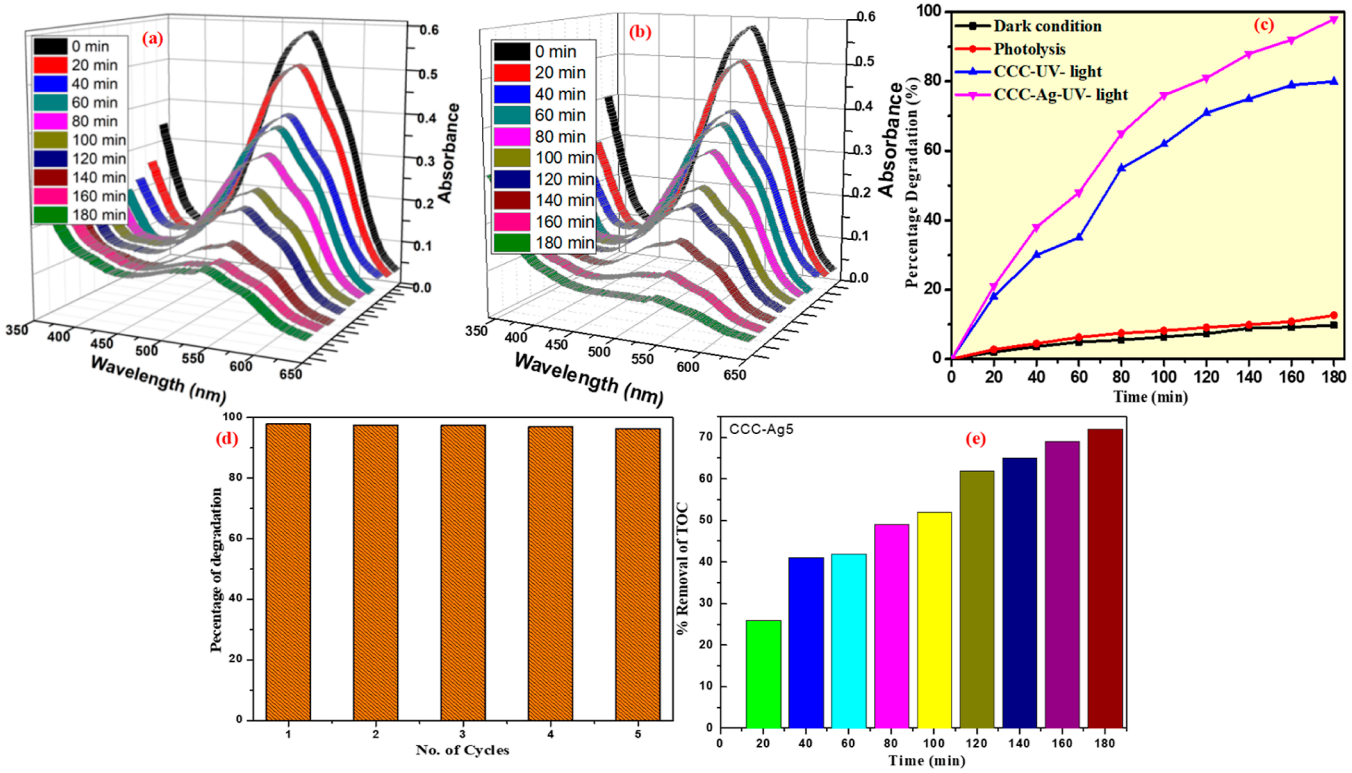

Figure 9. Change in absorbance of 40 ppm AR dye for (a) prepared C3 and (b) prepared C3Ag5 nanocomposites on AR dye; (c) photodegradation (%) for AR dye in the presence of C3Ag5 nanocomposites after sunlight irradiation for 180 min; and (d) stability performance and (e) TOC plot of C3Ag5.

Table 2. Standard Error of Spectral Absorbance Plots for AR Dye in the Presence of a Photocatalyst

sl. no.	standard error
0 min	8.44019×10^{-5}
20 min	6.46067×10^{-5}
40 min	6.42×10^{-5}
60 min	6.40695×10^{-5}
80 min	4.08217×10^{-5}
100 min	3.39352×10^{-5}
120 min	3.17071×10^{-5}
140 min	2.7848×10^{-5}
160 min	2.4329×10^{-5}
180 min	2.30896×10^{-5}

$$Ag(CuO - Cu_2O)Cu(e^-) + O_2 \rightarrow O^{2\bullet-}(\text{superoxide radical}) \quad (7)$$

$$O^{2\bullet-} + H_2O \rightarrow OH^\bullet + OH^- \quad (8)$$

5. ELECTROCHEMICAL INVESTIGATIONS OF C3 AND C3AG5 NANOCOMPOSITES

The electrochemical analysis was performed in a combination of three electrodes with 1.0 M KCl as the aqueous electrolyte at room temperature. Analysis techniques includeing cyclic voltammetry (CV), galvanostatic charge and discharge (GCD) tests, electrochemical impedance spectroscopy (EIS), and sensor studies were conducted. The specific capacitance (Scp) can be evaluated for the synthesized electrode from CV by eq 9.

$$\text{Scp} = \frac{\int I \, dV}{v \times m \times \Delta V} \quad (9)$$

where I—current, V—potential, m—electrode mass, v—scan rate, and ΔV—operating voltage window. From the charge–discharge curves, the Scp for the synthesized electrode was evaluated by eq 10.

$$\text{Scp} = I \times \Delta t / m \times \Delta V \quad (10)$$

where Δt is the discharge time. The energy density (E; W h/kg) and power density (P; W/kg) were estimated by eqs 11 and 12, respectively.

$$E = \frac{\text{Scp} \times \Delta V^2}{8 \times 3.6} \quad (11)$$

$$P = 3600 \times E/\Delta t \quad (12)$$

where Scp is the resulted specific capacitance from GCD studies.

Electrochemical performance of C3 and C3Ag5 was assessed through CV and GCD experiments by a three-electrode system. The CV curves of C3 and C3Ag5 at a scan rate of 0.02 V/s are given in Figure 12a (inset), which confirms the pseudocapacitive behavior with a couple of redox peaks over the cationic and anionic segments. C3Ag5 displayed a higher space area below the CV curve, signifying a higher value of Scp of 134 F/g than that of C3 (90.0 F/g). Figure 12a displays the CV curves of the C3Ag5 electrode at various scan rates. The curve validated that the shape of the CV curves progressively shifted and sloped along with the increase of the scan rate, and it maintained the redox position and electrochemical stability even when the scan rate increases. The Scp values of the

https://doi.org/10.1021/acsomega.2c07124
ACS Omega 2023, 8, 9947−9961

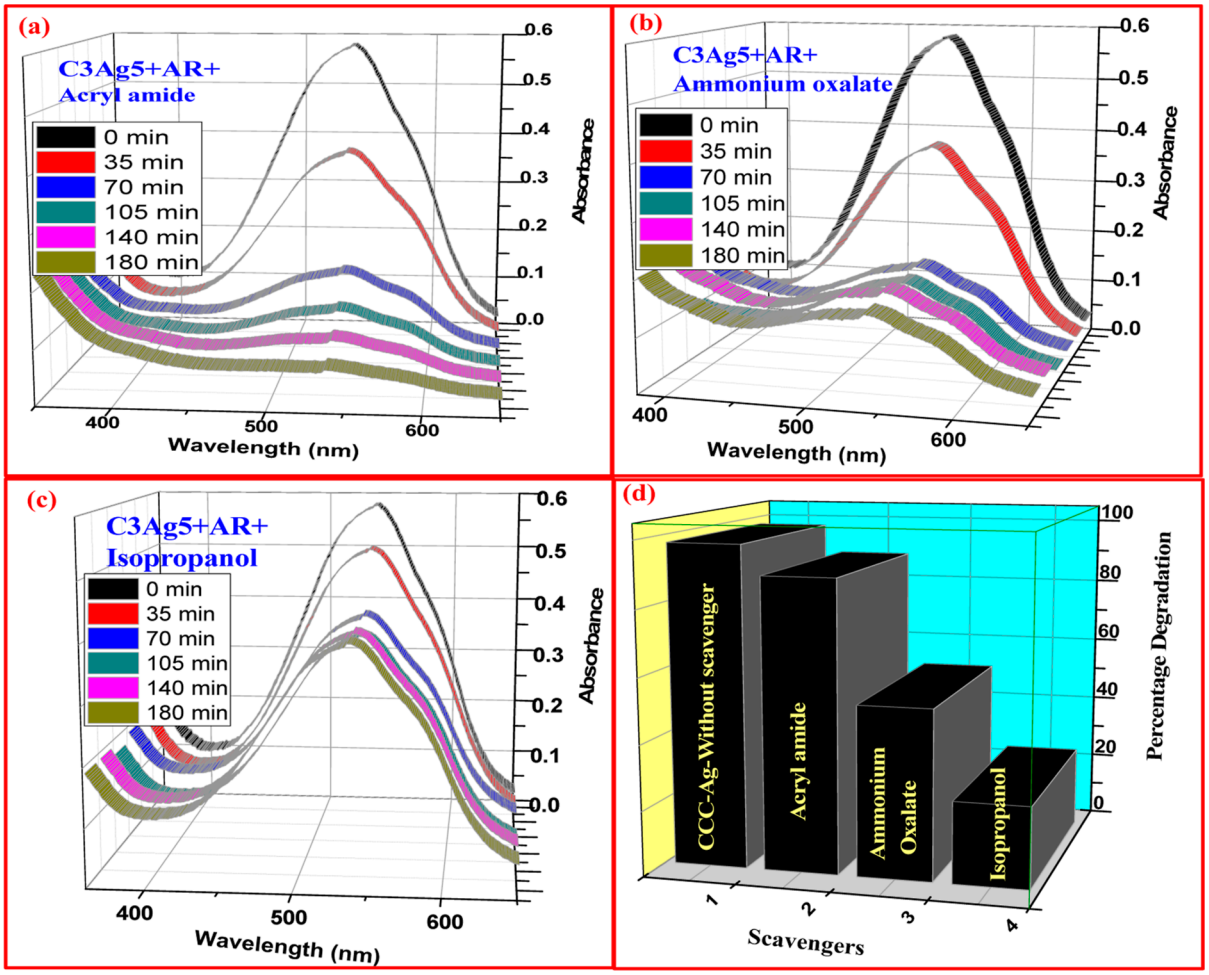

Figure 10. Variation of % concentration of AR dye under sunlight irradiation for the C3Ag5 photocatalyst in the presence of (a) AA; (b) AO; and (c) IP scavengers and (d) scavenger analysis plot.

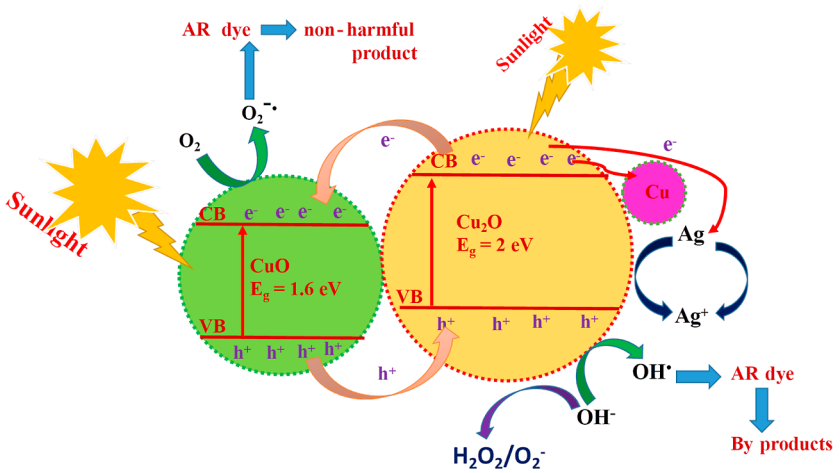

Figure 11. Probable mechanisms for photocatalytic degradation of AR dye by the C3Ag5 nanocomposite.

C3Ag5 electrode at 0.01, 0.02, 0.03, 0.04, and 0.05 V/s scan rates were 178.68, 134.01, 110.31,100.45, and 94.28 F/g, respectively. The Scp values decreased due to the slower penetration of the electrolytic ions into the pores of the sample at a higher scan rate.[46]

The GCD curves of C3 and C3Ag5 at a current density of 0.5 A/g is displayed in Figure 13a and it is in good agreement with the pseudocapacitive nature of linear triangular shapes. The Scp values for the C3 and C3Ag5 electrodes determined from the charge discharge curves at a current density of 0.5 A/g were 109.8 and 163.2 F/g, respectively. From Figure 13a and by the Scp values, it was confirmed that C3Ag5 shows better results than C3Ag^0. A cycling life of longer time with better stability is a crucial factor of supercapacitors.[43] Hence, the

https://doi.org/10.1021/acsomega.2c07124
ACS Omega 2023, 8, 9947−9961

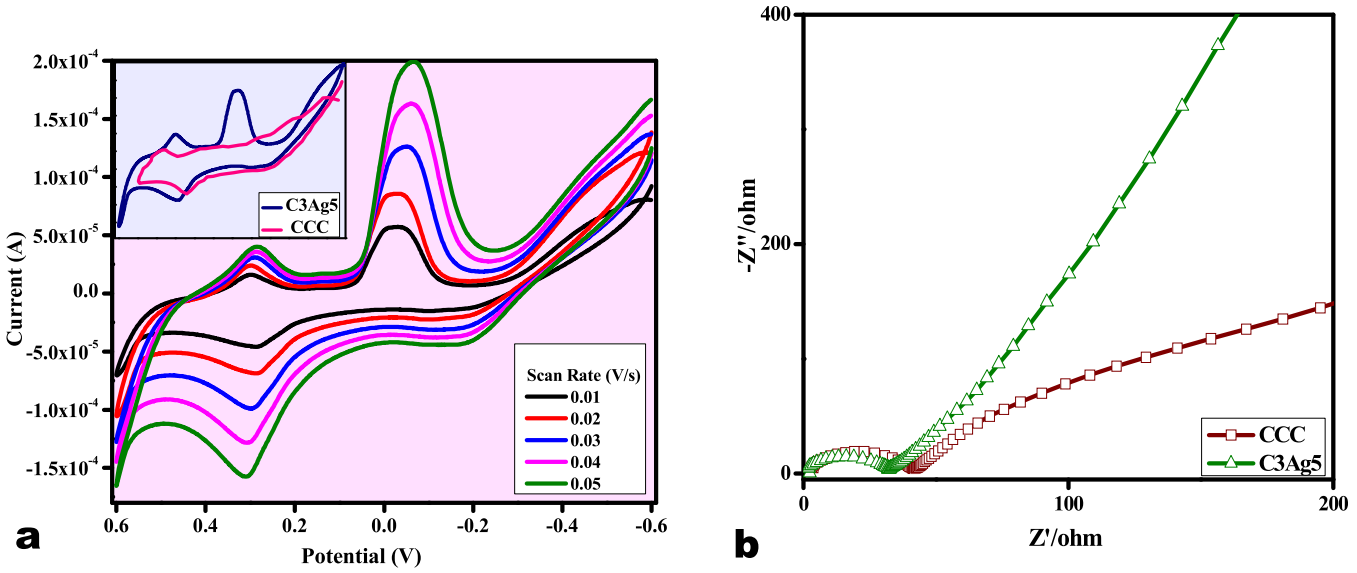

Figure 12. (a) CV curves of C3Ag5 at different scan rates, with the inset showing CV curves of C3Ag0 and C3Ag5. (b) Nyquist plots of C3 and C3Ag5.

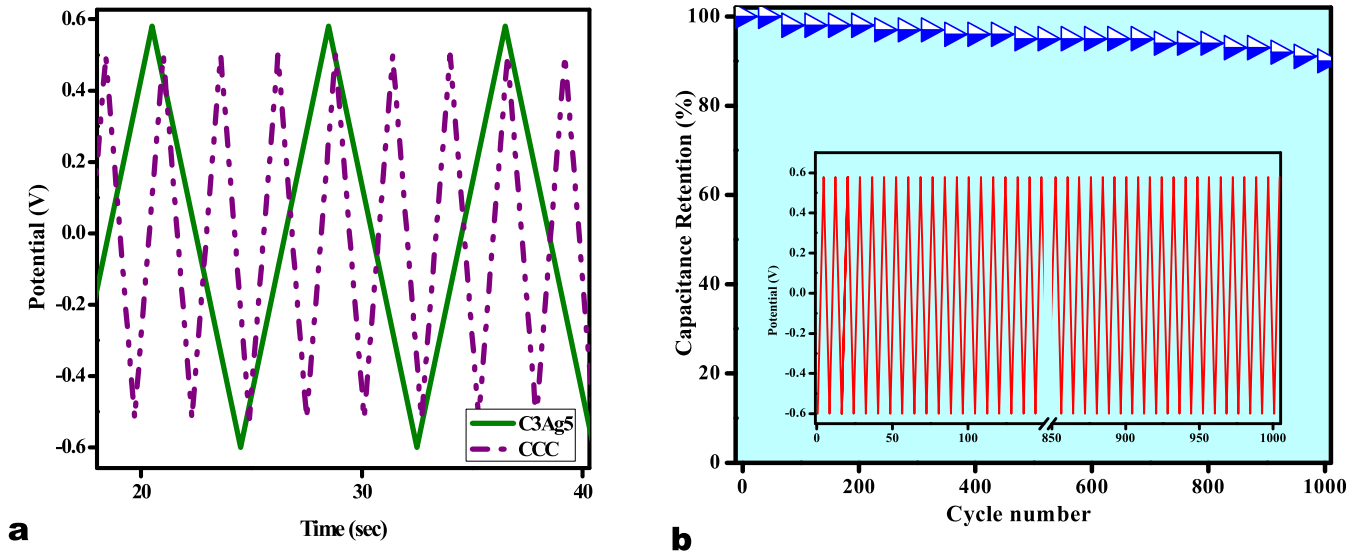

Figure 13. (a) GCD curves of C3 and C3Ag5 and (b) cycle capacitance retention in % of C3Ag5, with the inset showing the GCD cycle graph of C3Ag5.

capacitive retention cycle for the C3Ag5 electrode was conducted, which withstood till 1000 charge−discharge cycles and retained its capacitance at ∼ 90%, as depicted in Figure 13b, provinf the outstanding cycle stability. The obtained results confirmed the excellent cyclic stability and better energy density (10.5 W h/kg) at a power density of 474.3 W/kg.

EIS analysis was performed to know the electrochemical nature of the supercapacitor electrodes. Figure 12b displays the Nyquist curves of C3Ag0 and C3Ag5, which revealed a unique supercapacitor nature, having a quasi-circle present in the high-frequency area and a slanting line present in the low-frequency area.[47] The diameter estimated from the quasi-circle entails the charge transfer resistance (R_{ct}) as electrolytic solution persuading toward the electrode.[48] C3Ag5 results in a smaller R_{ct} (31 Ω) than C3Ag0 (43 Ω), validating the huge ion migration ratio at the boundary between the electrolytic solution and electrode.[49] Both the electrodes have vertical tails present in the low-frequency range due to enhanced ionic accessibility of the electrolyte to intercalate into the internal pores.

We have extended the electrochemical studies for the prepared electrodes using graphite toward sensor applications. In this point of view, we have utilized these electrodes to identify the presence of paracetamol in 0.1 M KCl electrolyte. Figure 14 (inset) explains the CV analysis of the C3Ag5 electrode for detecting paracetamol of concentrations 0 and 1 mM in the potential range (−1.0 to +1.0 V). As represented in Figure 14 (inset), the sensing of paracetamol in the electrolyte was confirmed by the change in the appearance of new oxidation and reduction potential peaks as compared to that for the bare electrolyte. The sensibility and stability were further confirmed by increasing the concentration of paracetamol in the electrolyte by the electrode, as shown in Figure 14. Hence, we can conclude that the novel nanoparticle C3Ag5 could act as a good sensor electrode.

https://doi.org/10.1021/acsomega.2c07124
ACS Omega 2023, 8, 9947−9961

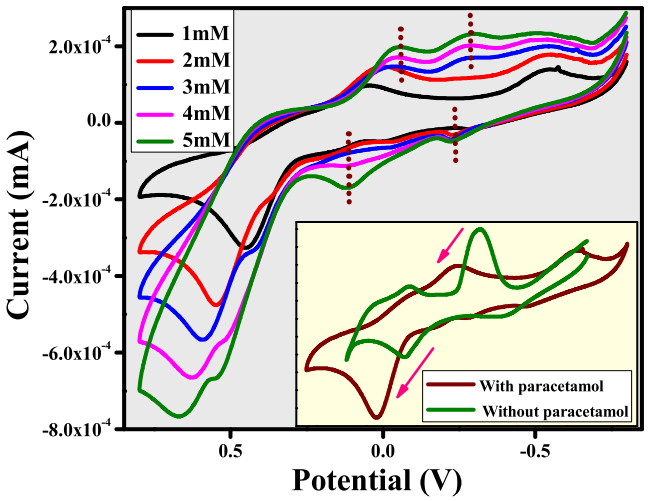

Figure 14. CV curves of different molar variations for sensing paracetamol, with the inset showing the CV curves of C3Ag5 with and without paracetamol.

5.1. Limit of Detection, Selectivity, Repeatability, and Stability. Figure 15 shows the linear variation with the paracetamol concentration in the range 1−5 mM calculated by using the following eq 13

$$I\ (\mathrm{mA}) = 0.028 \times (\mathrm{mM}) + 0.00000645\ (R = 0.96702) \quad (13)$$

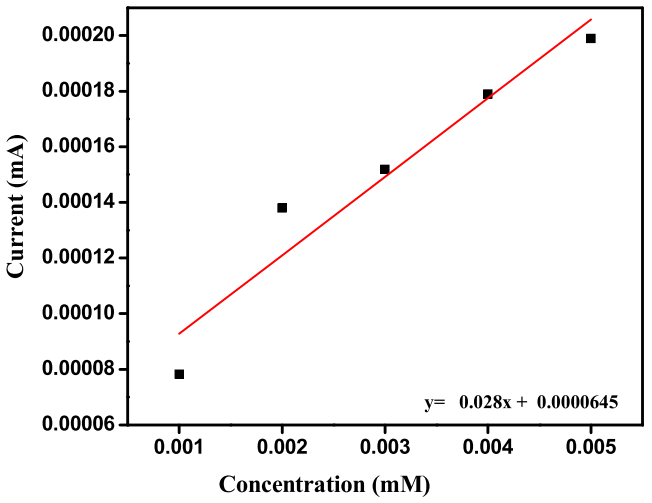

Figure 15. Plot of peak current vs paracetamol concentration.

The limit of detection was estimated to be 0.505 mM using $3\sigma/b$, where σ is the standard deviation of the blank and b is the slope of the calibration curve (sensitivity).

The C3Ag5 electrode was investigated for its selectivity toward paracetamol by introducing common interfering species under the conditions optimized for measurement. We considered electroactive species that may be present in pharmaceutical formulations and environmental samples.[50] These include organic compounds like sucrose, glucose, ascorbic acid, caffeine, and methanol, as well as some cations such as NH, Ca, and Ni.[51] The effect of these species on the oxidation peak was evaluated at a concentration of 5 mM paracetamol and a concentration of the interferent of 100 mM (i.e., 20 times that of paracetamol). We found no significant effect of these interfering substances, with the signal deviation remaining below ±10%. Thus, the C3Ag5 electrode offers satisfactory selectivity and can be effectively used for the determination of paracetamol in the presence of these common interfering substances.

The repeatability of the modified electrodes was also studied by measuring the peak current for 5 mM paracetamol with the same (already used) electrode with five repetitions. The relative standard deviation (RSD) of 3.5% was obtained, which indicated that the proposed electrode can be used multiple times for consecutive measurements. The evaluation of the long-tern storage stability of the modified electrode for 20 days was conducted by using the same electrode for a daily measurement of the peak current of 5 mM paracetamol. After 20 days, the peak current had only decreased by approximately 8.5% compared to the signal on the first day, while the RSD for the peak currents was 3.38%.

6. ANTIBACTERIAL MECHANISM

The synthesized nanocomposites were tested for antibacterial effectiveness against *E. coli* (Gram negative) and *S. aureus* (Gram positive). Figure 16 shows the zone of inhibition for C3

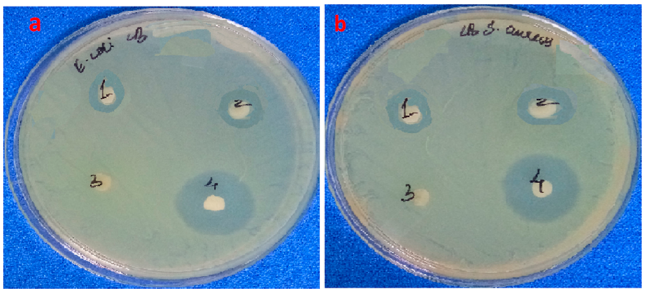

Figure 16. Antibacterial activity of nanocomposites, (a) *E coli* (b) *S. aureus*—1. C3 2. C3Ag5 (3.0 mg/mL) 3. Negative control 4. Positive control (Ciprofloxacin).

and C3Ag5 on *E. coli* and *S. aureus* bacteria by selecting *Ciprofloxacin* as the positive control. Table.3 shows the inhibitory zones of both the samples measured in millimeters. Due to the presence of Ag as the dopant in C3Ag5, its bacterial action against both Gram-positive and Gram-negative bacteria is increased.

The improved antibacterial activity of the C3Ag5 nanocomposite is attributed to its smaller size, and it can easily penetrate the cell wall and cause structural changes such as perforation, resulting in the leakage of intracellular components; additionally, the C3Ag5 nanocomposite releases the Ag^+ ion upon reaching the interior, generating reactive oxygen species that interact with membrane proteins, affecting the electron transport chain.[52] The C3Ag5 composite exhibited high antibacterial performance compared to C3, and this could be due to the presence of various reactive oxygen species on the photocatalyst, as result of which it disrupts the cell wall of the bacteria. Under the impact of such reactive species, bacterial cells may die due to lipid peroxidation, which causes the cell membrane structure to break down.[53−56] The antibacterial activity of these studies is compared with that in the other reported work as given in Table.4.

https://doi.org/10.1021/acsomega.2c07124
ACS Omega 2023, 8, 9947−9961

Table 3. Zone of Inhibition for C3-Ag and C3 Nanocomposites

C3Ag5				C3			
E. coli	*S. aureus*	positive control	negative control	*E. coli*	*S. aureus*	positive control	negative control
19 mm	18 mm	22 mm	00 mm	17 mm	16 mm	22 mm	00 mm

Table 4. Comparison of Antibacterial Activity with Reported Data

compound	bacteria	zone of inhibition (mm)	reference no.
Ag-doped $(CuO/Cu_2O)Cu$	*E. coli*	17	current study
	S. aureus	16	
Ag-doped TiO2@SiO2	*E. coli*	18	53
	S. aureus	16	
Ag-doped TiO2−MWCNT	*E. coli*	15	54
Ag-doped ZnO	*E. coli*	12	55
	S. aureus	13	
Ag-doped Fe_3O_4	*E. coli*	21	56
	S. aureus	12	

7. CONCLUSIONS

The heterostructure of Ag-doped $(CuO−Cu_2O)Cu$ nanocomposites were prepared by a solution combustion route using green *L. aspera* extract as a fuel. The structural analysis of the host and Ag-doped $CuO/Cu_2O/Cu$ samples were examined by PXRD spectra for the confirmation of the existence of CuO, Cu_2O, and metallic Cu as distinct phases. As the Ag content is increased from 0 to 7 mol %, the broadening of the peaks of (002) and (111) planes of CuO gradually occurs, which indicates the smaller crystallite size of the material, and the transformation phase of Cu_2O to CuO in $(CuO−Cu_2O)Cu$ along the planes was observed. The existence of Ag in the $(CuO−Cu_2O)$ Cu nanocomposite is confirmed by the existence of two peaks of Ag $3d_{5/2}$ (367.9 eV) and Ag $3d_{3/2}$ (373.9 eV) in the XPS spectrum. Photocatalytic dye degradation activity of the prepared doped nanocomposite was examined, and an excellent AR dye degradation of 98% at 90 min was achieved. The electrochemical analysis was performed for prepared electrodes using graphite in a combination of three electrodes with 1 M KCl, which showed excellent sensing of paracetamol medicinal chemical, confirmed by the appearance of new redox potential peaks as compared to that in the bare electrolyte spectrum. Further, the increasing antibacterial activity of the C3Ag5 nanocomposite against *E. coli* and *S. aureus* showed improved performance, which was attributed to the presence of Ag as a dopant. The reported research provides better insights into the development of multifunctional applications of nanocomposites using doping practice.

AUTHOR INFORMATION

Corresponding Authors

Kurupalya Shivram Anantharaju − *Department of Chemistry, Dayananda Sagar College of Engineering, Bengaluru 560111, India; Dr. D. Premachandra Sagar Centre for Advanced Materials (Affiliated to Mangalore University), DSCE, Bengaluru 560111, India*; Email: iamananthkurupalya@gmail.com

B. S. Surendra − *Department of Chemistry, Dayananda Sagar College of Engineering, Bengaluru 560111, India*; Email: surendramysore2010@gmail.com

H. C. Ananda Murthy − *Department of Applied Chemistry, School of Applied Natural Sciences, Adama Science and Technology University, Adama 1888, Ethiopia; Department of Prosthodontics, Saveetha Dental College & Hospital, Saveetha Institute of Medical and Technical Science (SIMATS), Saveetha University, Chennai 600077 Tamil Nadu, India*; orcid.org/0000-0002-2361-086X; Email: anandkps350@gmail.com

Authors

B. Uma − *Department of Chemistry, Dayananda Sagar College of Engineering, Bengaluru 560111, India*

K. Gurushantha − *Department of Chemistry, M S Ramaiah Institute of Technology, Bengaluru 560054 Karnataka, India*

Sunil S. More − *School of Basic and Applied Sciences, Dayananda Sagar University, Bangalore 560111, India*

S. Meena − *Department of Chemistry, Dayananda Sagar College of Engineering, Bengaluru 560111, India*

B. Hemavathi − *Department of Chemistry, Dayananda Sagar College of Engineering, Bengaluru 560111, India*

Complete contact information is available at: https://pubs.acs.org/10.1021/acsomega.2c07124

Author Contributions

B.U.: investigation, methodology, and writing—original draft. K.S.A.: conceptualization, methodology, project administration, supervision, and writing—reviewing and editing. K.G.: methodology and analysis. B.S.S.: data curation and writing—reviewing and editing. S.S.M.: data curation and formal analysis. S.M.: methodology. B.H.: experimentation. H.C.A.M.: writing—reviewing and editing.

Notes

The authors declare no competing financial interest.

ACKNOWLEDGMENTS

The authors are grateful to the managements of Dayananda Sagar College of Engineering, India, and Adama Science and Technology University, Ethiopia. The authors also thank Dr. Vidya Yalekadakalu Shivanna for providing analytical support to this work.

REFERENCES

(1) Iqbal, S.; Javed, M.; Ali, B.; Azam Qamar, M.; Ahmad, M.; Shoaib, M.; Raheel, M.; Ahmad, N.; Akbar, M. B.; Li, H. Controlled synthesis of Ag doped CuO nanoparticles as a core with poly(acrylic acid) microgel shell for efficient removal of methylene blue under visible light. *J. Mater. Sci.: Mater. Electron.* **2020**, *9*, 03377.

(2) Menazea, A. A.; Mostafa, A. M. Ag doped CuO thin film prepared via Pulsed Laser Deposition for 4-nitrophenol degradation. *J. Environ. Chem. Eng.* **2020**, *8*, 104104.

(3) Gouvêa, C. A.; Wypych, F.; Moraes, S. G. Semiconductor-assisted photodegradation of lignin, dye, and kraft effluent by Ag-doped ZnO. *Chemosphere* **2000**, *40*, 427−432.

(4) Absike, H.; Hajji, M.; Labrim, H.; Abbassi, A.; Ez-Zahraouy, H. Electronic, electrical and optical properties of Ag doped CuO through modified Becke-Johnson exchange potential. *Superlattices Microstruct.* **2017**, *17*, 128.

(5) Gupta, K.; Singh, R. P.; Pandey, A.; Pandey, A. Photocatalytic antibacterial performance of TiO2 and Ag-doped TiO2 against S. aureus. P. aeruginosa and E. coli. *Beilstein J. Nanotechnol.* **2013**, *4*, 345−351.
(6) Bate, N.; Shi, H.; Chen, L.; Wang, J.; Xu, S.; Chen, W.; Li, J.; Wang, E.-B. Micelle-Directing Synthesis of Ag-Doped WO3 and MoO3 Composites for Photocatalytic Water Oxidation and Organic-Dye Adsorption. *Adsorption* **2017**, *12*, 2597−2603.
(7) Das, S.; Alford, T. L. Structural and optical properties of Ag-doped copper oxide thin films on polyethylene napthalate substrate prepared by low temperature microwave annealing. *J. Appl. Phys.* **2013**, *113*, 244905.
(8) Khurshid, F.; Jeyavelan, M.; Hudson, M. S. L.; Nagarajan, S. Ag-doped ZnO nanorods embedded reduced graphene oxide nano-composite for photo-electrochemical applications. *R. Soc. Open Sci.* **2019**, *6*, 181764.
(9) Turky, A. El-M. M.; Radwan, N. R. E.; El-Shobaky, G. A. Surface and catalytic properties of CuO doped with MgO and Ag_2O. *Colloids Surf., A* **2001**, *181*, 57−68.
(10) Xu, J.; Liu, B.; Song, Z.; Feng, S.; Chen, B. Crystallization and C-RAM application of Ag-doped Sb2Te3 material. *Mater. Sci. Eng., B* **2006**, *127*, 228−232.
(11) Uma, B.; Anantharaju, K. S.; Renuka, L.; Nagabhushana, H.; Malini, S.; More, S. S.; Vidya, Y. S.; Meena, S. Controlled synthesis of (CuO-Cu_2O)Cu/ZnO multi oxide nanocomposites by facile combustion route: A potential photocatalytic, antimicrobial and anticancer activity. *Ceram. Int.* **2021**, *47*, 14829−14844.
(12) Xu, Z.; Liu, L.; Sun, H.; Gao, C. Highly Electrically Conductive Ag-Doped Graphene Fibers as Stretchable. *Conductors* **2013**, *25*, 3249−3253.
(13) Yu, P.; Cui, B.; Chang, Z. Preparation and characterization of Ag-doped BaTiO3 based X7R ceramics. *Mater. Res. Bull.* **2009**, *44*, 893−897.
(14) Ahmed, S.; Ahmad, M.; Swami, B.; Ikram, S. A review on plants extract mediated synthesis of silver nanoparticles for antimicrobial applications: A green expertise. *J. Adv. Res.* **2016**, *7*, 17−28.
(15) Malleshappa, J.; Nagabhushana, H.; Sharma, S. C.; Vidya, Y. S.; Anantharaju, K. S.; Prashantha, S. C.; Daruka Prasad, B.; Raja Naika, H.; Lingaraju, K.; Surendra, B. S. Leucas aspera mediated multifunctional CeO_2 nanoparticles: Structural, Photoluminescent, Photocatalytic and Antibacterial properties. *Spectrochim. Acta, Part A* **2015**, *149*, 452−462.
(16) Sosnowska, M.; Adamiak, M.; Bugajska, A.; Daniluk, K.; Gawin, Z.; Kutwin, K. Green synthesis of silver nanoparticles by using aqueous mint (Mentha piperita) and cabbage (Brassica oleracea var. capitata) extracts and their antibacterial activity. *Ann. Warsaw Univ. Life Sci.–SGGW, Anim. Sci.* **2017**, *56*, 137−145.
(17) Renuka, L.; Anantharaju, K. S.; Vidya, Y. S.; Nagabhushana, H.; Uma, B.; Malini, S.; More, S. S.; Koppad, P. Porous network ZrO2/ZnFe2O4 nanocomposite with heterojunction towards industrial water purification under sunlight: Enhanced charge separation and elucidation of photo-mechanism. *Ceram. Int.* **2021**, *47*, 14845−14861.
(18) Li, J.; Chen, X.; Ai, N.; Hao, J.; Chen, Q.; Strauf, S.; Shi, Y. Silver nanoparticle doped TiO2 nanofiber dye sensitized solar cells. *Chem. Phys. Lett.* **2011**, *514*, 141−145.
(19) Yathisha, R. O.; Arthoba Nayaka, Y.; Manjunatha, P.; Purushothama, H. T.; Vinay, M. M.; Basavarajappa, K. V. Study on the effect of Zn2+ doping on optical and electrical properties of CuO nanoparticles. *Phys. E* **2019**, *108*, 257−268.
(20) Ansari, S. A.; Nisar, A.; Fatma, B.; Khan, W.; Naqvi, A. H. Investigation on structural, optical and dielectric properties of Co doped ZnO nanoparticles synthesized by gel-combustion route. *Mater. Sci. Eng., B* **2012**, *5*, 428−435.
(21) Kumar, P.; Chandra Mathpal, M.; Prakash, J.; Viljoen, B. C.; Roos, W. D.; Swart, H. C. Band gap tailoring of cauliflower-shaped CuO nanostructures by Zn doping for antibacterial applications. *J. Alloys Compd.* **2020**, *832*, 154968.
(22) Jiang, T.; Wang, Y.; Meng, D.; Wang, D. One-step hydrothermal synthesis and enhanced photocatalytic performance of pine-needle-like Zn-doped CuO nanostructures. *J. Mater. Sci.: Mater. Electron.* **2016**, *27*, 12884−12890.
(23) Arun, L.; Karthikeyan, C.; Philip, D.; Sasikumar, M.; Elanthamilan, E.; Merlin, J. P.; Unni, C. Effect of Ni2+ doping on chemocatalytic and supercapacitor performance of biosynthesized nanostructured CuO. *J. Mater. Sci.: Mater. Electron.* **2018**, *29*, 21180−21193.
(24) Luo, X.; Yuan, J.; Liu, Y.; Liu, C.; Zhu, X.; Dai, X.; Ma, Z.; Wang, F. Improved Solid-Phase Synthesis of Phosphorylated Cellulose Microsphere Adsorbents for Highly Effective Pb2+ Removal from Water: Batch and Fixed-Bed Column Performance and Adsorption Mechanism. *Chem. Eng.* **2017**, *5*, 5108−5117.
(25) Yang, J.; Luo, X. Ag-doped TiO2 immobilized cellulose-derived carbon beads: One-Pot preparation, photocatalytic degradation performance and mechanism of ceftriaxone sodium. *Appl. Surf. Sci.* **2021**, *542*, 148724.
(26) Akhavan, O.; Ghaderi, E. Cu and CuO nanoparticles immobilized by silica thin films as antibacterial materials and photocatalysts. *Surf. Coat. Technol.* **2010**, *205*, 219−223.
(27) Shaikh, J. S.; Pawar, R. C.; Devan, R. S.; Ma, Y. R.; Salvi, P. P.; Kolekar, S. S.; Patil, P. S. Synthesis and characterization of Ru doped CuO thin films for supercapacitor based on Bronsted acidic ionic liquid. *Electrochim. Acta* **2011**, *56*, 2127−2134.
(28) Uma, B.; Anantharaju, K. S.; Renuka, L.; Nagabhushana, H.; Malini, S.; More, S. S.; Vidya, Y. S.; Meena, S. Controlled synthesis of (CuO-Cu_2O)Cu/ZnO multi oxide nanocomposites by facile combustion route: A potential photocatalytic, antimicrobial and anticancer activity. *Ceram. Int.* **2021**, *47*, 14829−14844.
(29) Manibalan, G.; Murugadoss, G.; Thangamuthu, R.; Ragupathy, P.; Mohan Kumar, R.; Jayavel, R. Enhanced electrochemical supercapacitor and excellent amperometric sensor performance of heterostructure CeO2-CuO, nanocomposites via chemical route. *Appl. Surf. Sci.* **2019**, *456*, 104−113.
(30) Vinogradov, A. V.; Agafonov, A. V.; Vinogradov, V. V.; Davydova, O. I. Sol-gel synthesis of photochromic films via silver−titania nanocomposites prepared without heat treatment. *Mendeleev Commun.* **2012**, *22*, 27−28.
(31) Kubelka, P.; Munk, F. Ein Beitrag Zur Optik Der Farbanstriche. *Z. Tech. Phys.* **1931**, *12*, 593−601.
(32) Lakshmi Ranganatha, V.; Pramila, S.; Nagaraju, G.; Udayabhanu; Surendra, C.; Mallikarjunaswamy, C. Cost-effective and green approach for the synthesis of zinc ferrite nanoparticles using Aegle Marmelos extract as a fuel: catalytic, electrochemical, and microbial applications. *J. Mater. Sci.: Mater. Electron.* **2020**, *31*, 17386−17403.
(33) Ahmed, M. A.; El-Katori, E. E.; Gharni, Z. H. Photocatalytic degradation of methylene blue dye using Fe2O3/TiO2 nanoparticles prepared by sol−gel method. *J. Alloys Compd.* **2013**, *553*, 19−29.
(34) Bhadra, S.; Khastgir, D. Extrinsic and intrinsic structural change during heat treatment of polyaniline. *Polym. Degrad. Stab.* **2008**, *93*, 1094.
(35) Surendra, B. S. Green engineered synthesis of Ag-doped $CuFe_2O_4$: Characterization, cyclic voltammetry and photocatalytic studies. *J. Sci.: Adv. Mater. Devices* **2018**, *3*, 44−50.
(36) Surendra, B. S.; Veerabhdraswamy, M.; Anantharaju, K. S.; Nagaswarupa, H. P.; Prashantha, S. C. Green and chemical engineered $CuFe_2O_4$: Characterization, Cyclic Voltammetry, Photocatalytic and Photoluminescent investigation for multifunctional applications. *J. Nanostruct. Chem.* **2018**, *8*, 45−59.
(37) Surendra, B. S.; Veerabhadraswamy, M. Microwave assisted synthesis of polymer via bioplatform chemical intermediate derived from Jatropha deoiled seed cake. *J. Sci.: Adv. Mater. Devices* **2017**, *2*, 340−346.
(38) Surendra, B. S.; Veerabhadraswamy, M.; Anil kumar, H. G.; Kendagannaswamy, B. K.; Nagaswarupa, H. P.; Prashanth, S. C. Microwave assisted synthesis of Schiff base via bioplatform chemical intermediate (HMF) derived from Jatropha deoiled seed cake catalyzed by modified Bentonite clay. *J. Mater. Today* **2017**, *4*, 11727−11736.

https://doi.org/10.1021/acsomega.2c07124
ACS Omega 2023, 8, 9947−9961

(39) Saleh, R.; Djaja, N. UV light photocatalytic degradation of organic dyes with Fe-doped ZnO nanoparticles. *Superlattices Microstruct.* **2014**, *74*, 217−233.
(40) Saravanan, R.; Karthikeyan, S.; Gupta, V. K.; Sekaran, G.; Narayanan, V.; Stephen, A. Enhanced photocatalytic activity of ZnO/CuO nanocomposite for the degradation of textile dye on visible light illumination. *Mater. Sci. Eng., C* **2013**, *33*, 91−98.
(41) Fang, H.; Guo, Y.; Wu, T.; Liu, Y. Biomimetic synthesis of urchin-like CuO/ZnO nanocomposites with excellent photocatalytic activity. *New J. Chem.* **2018**, *42*, 12779−12786.
(42) Zhang, J.; Chen, T.; Yu, J.; Liu, C.; Yang, Z.; Lu, H.; Yin, F.; Gao, J.; Liu, Q.; Zhang, X.; Tu, Y. Enhanced photocatalytic activity of flowerlike CuO-ZnO nanocomposites synthesized by one-step hydrothermal method. *J. Mater. Sci.: Mater. Electron.* **2016**, *27*, 10667−10672.
(43) Hegde, S. S.; Bose, R. S. C.; Surendra, B. S.; Vinoth, S.; Murahari, P.; Ramesh, K. SnS-Nanocatalyst: Malachite green degradation and electrochemical sensor studies. *Mater. Sci. Eng., B* **2022**, *283*, 115818.
(44) Structural and optical properties of MgNb2O6 NPs: Its potential application in photocatalytic and pharmaceutical industries as sensor Basavaraju, N.; Prashantha, S. C.; Surendra, B. S.; Shashi Shekhar, T. R.; Anil Kumar, M. R.; Ravikumar, C. R.; Raghavendra, N.; Shashidhara, T. S. Structural and optical properties of MgNb2O6 NPs: Its potential application in photocatalytic and pharmaceutical industries as sensor. *Environ. Nanotechnol., Monit. Manage.* **2021**, *16*, 100581.
(45) Uma, B.; Anantharaju, K. S.; Renuka, L.; Nagabhushana, H.; Malini, S.; More, S. S.; Vidya, Y. S.; Meena, S. Controlled synthesis of (CuO-Cu2O)Cu/ZnO multi oxide nanocomposites by facile combustion route: A potential photocatalytic, antimicrobial and anticancer activity. *Ceram. Int.* **2020**, *47*, 14829.
(46) Norouzi, O.; Pourhosseini, S. E. M.; Naderi, H. R.; Di Maria, F.; Dutta, A. Integrated Hybrid Architecture of Metal and Biochar for High Performance Asymmetric Supercapacitors. *Sci. Rep.* **2021**, *11*, 5387.
(47) Cao, Y.; Yang, W.; Wang, M.; Wu, N.; Zhang, L.; Guan, Q.; Guo, H. Metalorganic Frameworks as Highly Efficient Electrodes for Long Cycling Stability Supercapacitors. *Int. J. Hydrogen Energy* **2021**, *46*, 18179−18206.
(48) Liu, R.; Pan, L.; Liu, X.; Wu, D. An Evaporation-Induced Triconstituent Assembly Approach to Fabricate an Ordered Mesoporous Carbon/graphene Aerogel for High-Performance Supercapacitors. *RSC Adv.* **2015**, *5*, 16765−16768.
(49) Yoo, H. D.; Jang, J. H.; Ryu, J. H.; Park, Y.; Oh, S. M. Impedance Analysis of Porous Carbon Electrodes to Predict Rate Capability of Electric Double-Layer Capacitors. *J. Power Sources* **2014**, *267*, 411−420.
(50) Wang, H.; Yu, S.; Xu, B. Hierarchical Porous Carbon Materials Prepared Using Nano-ZnO as a Template and Activation Agent for Ultrahigh Power Supercapacitors. *Chem. Commun.* **2016**, *52*, 11512−11515.
(51) Alam, A. U.; Qin, Y.; Howlader, M. M. R.; Hu, N.-X.; Deen, M. J. Electrochemical sensing of acetaminophen using multi-walledcarbon nanotube and β-cyclodextrin. *Sens. Actuators, B* **2018**, *254*, 896−909.
(52) Pinyou, P.; Blay, V.; Chansaenpak, K.; Lisnund, S. Paracetamol Sensing with a Pencil Lead Electrode Modified with Carbon-Nanotubes and Polyvinylpyrrolidone. *Chemosensors* **2020**, *8*, 133.
(53) Govindhan, P.; Pragathiswaran, C. Antibacterial Activity and Anticancer Activity of Ag Doped TiO_2@SiO_2 Nanocomposite. *J. Nanosci. Nanotechnol.* **2016**, *3*, 173−175.
(54) Hossain, M. A.; Elias, M.; Sarker, D. R.; Diba, Z. R.; Mithun, J. M.; Azad, M. A. K.; Siddiquey, I. A.; Rahman, M. M.; Uddin, J. Synthesis of Fe- or Ag-doped TiO_2−MWCNT nanocomposite thin films and their visible-light-induced catalysis of dye degradation and antibacterial activity. *Res. Chem. Intermed.* **2018**, *18*, 3253.
(55) Hou, Y.; Feng, J.; Wang, Y.; Li, L. Enhanced antibacterial activity of Ag-doped ZnO/polyaniline nanocomposites. *J. Mater. Sci.: Mater. Electron.* **2016**, *27*, 6615.
(56) Babu, A. T.; Sebastian, M.; Manaf, O.; Antony, R. Heterostructured Nanocomposites of Ag Doped Fe_3O_4 Embedded in ZnO for Antibacterial Applications and Catalytic Conversion of Hazardous Wastes. *J. Inorg. Organomet. Polym. Mater.* **2019**, *30*, 1944.

https://doi.org/10.1021/acsomega.2c07124
ACS Omega 2023, 8, 9947−9961